A Dual-Side Variable Duty Cycle Phase-Shift Modulation Strategy for DAB Converter With Minimal Current Stress

Shanshan Gao, *Senior Member, IEEE*, Jiaran Xu, Yijie Wang, *Senior Member, IEEE*, Xiangjun Zhang, *Member, IEEE*, Jianxing Liu, *Senior Member, IEEE*, Cong Huang, and Dianguo Xu, *Fellow, IEEE*

***Abstract*—Nowadays, dual active bridge (DAB) converters are widely used due to the advantages of wide voltage regulation range, high efficiency, and easy realization of soft switching. In order to ensure the efficient operation of DAB, there are increasing studies on three degrees of freedom modulation schemes, but the problems of high current stress and narrow soft switching range especially in light load range still affect the performance of DAB. Therefore, a dual-side variable duty cycle phase-shift modulation (DVDM) is proposed in this article, in which the duty cycles of the primary and secondary side switches of DAB change simultaneously. Lagrange multiplier method and Karush–Kuhn–Tucker conditions are utilized to optimize the peak-to-peak inductor current under DVDM control, and obtains a complete optimized modulation scheme. By comparing the RMS current and soft switching characteristics of DVDM control with existing three degrees of freedom modulation schemes, the advantages of the DVDM control can be proved. Finally, a 250 W experimental prototype with 50 V input and 25 V output is built under 100 kHz switching frequency to verify the above analysis. The obtained peak efficiency is up to 95.48%.**

***Index Terms*—Dual active bridge (DAB), dual-side variable duty cycle modulation (DVDM), peak-to-peak inductor current, soft switching.**

I. Introduction

COMPARED to ac microgrids, dc microgrids have higher efficiency, lower complexity of control systems, and better connectivity with many types of energy storage systems and renewable energy sources [1]. Therefore, dc microgrids are widely used and have great potential of development. The bidirectional dc–dc converter is one of the critical equipment of the dc microgrids, which plays an important role in the bidirectional flow of energy and the maintenance of system power balance. Dual active bridge (DAB) converter has become a commonly used topology in isolated bidirectional dc–dc converters due to its advantages of wide voltage regulation range, bidirectional isolation, high power density, and easy implementation of soft switching. Moreover, it has good application prospects in photovoltaics [2], electric vehicles [3], and aerospace [4].

The traditional control method of DAB is phase-shift modulation, which controls the transmission power by varying the phase difference of the driving signals between different bridge arms. Single-phase-shift (SPS) control can only adjust the phase-shift angle between the full-bridges of the primary and secondary sides, so the control method is simple. However, under light load or voltage mismatch conditions, most switches can only achieve hard switching, which may lead to high reactive power and low efficiency [5]. Hence, researchers have proposed control strategies with more degrees of freedom to improve the performance of DAB [6], [7], [8], [9]. Extended-phase-shift (EPS) control and dual-phase-shift (DPS) control are generally used in the modulation scheme with two degrees of freedom. The two full-bridges under DPS control have the same intra bridge phase-shift. In [10], a current stress optimization control strategy under DPS is proposed, which can greatly reduce the current stress to improve efficiency, but it does not take the soft switching characteristics into account. The characteristic of EPS control is that only one side of the full-bridge has an inner phase-shift ratio. By using Karush–Kuhn–Tucker (KKT) conditions to minimize the backflow power [11], the efficiency is improved over a wide operating range while decreasing current stress. Nevertheless, the ZVS range at different power levels is relatively limited.

Triple-phase-shift (TPS) control is a typical three degrees of freedom control strategy [12], [13], [14], [15], which has flexible control methods and multiple schemes to optimize characteristics such as current stress, RMS current, ZVS range, etc. Fundamental duty modulation (FDM) proposed in [15] is also one of TPS control methods, which utilizes the fundamental component analysis model to figure out the optimal solution that minimizes the inductor current, so as to achieve the purpose of improving the ZVS range and efficiency of DAB. However, at

Received 15 January 2025; revised 18 March 2025; accepted 18 April 2025. Date of publication 22 April 2025; date of current version 30 June 2025. This work was supported in part by the National Nature Science Foundation of China under Grant 52207194, in part by the Heilongjiang Province Postdoctoral Science Foundation under Grant LBH-Z22023, in part by Young Elite Scientist Sponsorship Program by CSEE under Grant JLB2023246. Recommended for publication by Associate Editor M. Ponce-Silva. *(Corresponding author: Shanshan Gao.)*

Shanshan Gao, Jiaran Xu, Yijie Wang, Xiangjun Zhang, and Dianguo Xu are with the School of Electrical Engineering and Automation, Harbin Institute of Technology, Harbin 150000, China. (e-mail: gaoshanshan@hit.edu.cn; 24s106261@stu.hit.edu.cn; wangyijie@hit.edu.cn; xiangjunzh@hit.edu.cn; xudiang@hit.edu.cn).

Jianxing Liu is with the School of Astronautics, Harbin Institute of Technology, Harbin 150001, China. (e-mail: jx.liu@hit.edu.cn).

Cong Huang is with the School of Mechatronics Engineering, Harbin Institute of Technology, Harbin 150001, China. (e-mail: huangc@hit.edu.cn).

Color versions of one or more figures in this article are available at https://doi.org/10.1109/TPEL.2025.3563577.

Digital Object Identifier 10.1109/TPEL.2025.3563577

light-load conditions, the RMS current is higher than traditional TPS control which results in limitation of the improvement in efficiency. Among the control strategies mentioned above, the duty cycle of all switches is 50%, and the working waveforms within half switching period are symmetrical, so they can also be called as symmetrical duty modulation (SDM).

With the continuous deepening of the research on traditional modulation schemes, researchers found that symmetrical inductor current waveform under SDM may lead to serious circulating power losses [16]. Many strategies optimize the inductor RMS current [17], [18] or reactive power [19], [20], but it is difficult to achieve ZVS for all switches in the full load range, especially, the efficiency in low power range also needs to be improved. Therefore, asymmetric duty modulation (ADM) schemes with duty cycle less than 50% have been proposed [21], [22], [23]. ADM schemes are first used in dual active half-bridge (DAHB) converters. In [22] and [23], ADM with two degrees of freedom and three degrees of freedom for DAHB are proposed respectively, in which the duty cycles on both sides of the transformer can be changed, and the RMS current is minimized under a given power. It is found that the ZVS ability under light load is improved, and the efficiency advantage is significant. In [24], an optimization scheme of ADM for DAB is discussed, in which the full-bridge output voltage only has one continuous zero-voltage period in one switching period. Based on the ADM scheme, the peak-to-peak inductor current is optimized to obtain the optimal asymmetric duty modulation (OADM) scheme. The results show that compared with SDM scheme, the ZVS range is amplified, in addition, the current-related losses are reduced, and the efficiency at light load conditions is increased by 2.5%–28.57%. Although the number of soft switches is increased, there are still five switches cannot be soft switched at light load. Chen et al. [25] propose a modulation strategy with asymmetric compression duty cycle, which significantly reduces the RMS current and current stress under light load, but there is a large loss in the soft switching range and efficiency under heavy load.

Due to the issues of high current stress or narrow ZVS range in the previously proposed modulation schemes, this article proposes a dual-side variable duty cycle phase-shift modulation (DVDM) control strategy based on EPS control and ADM control, which has three degrees of freedom. Diverse from the previous ADM scheme, the primary and secondary full-bridges are driven by the same variable duty cycle pulsewidth modulation (PWM) signal, so DVDM scheme actually controls four variables with three degrees of freedom, which contributes to better control performance without increasing control complexity. Apart from the outer phase-shift angle between the two full-bridges, there is an inner phase-shift in the primary full-bridge. EPS control can be regarded as a special case of this control strategy when the duty cycle of all switches is 50%. By optimizing the peak-to-peak inductor current, the RMS current can also be greatly reduced, which is lower than that of the previous mentioned FDM and OADM schemes. In the high power range, all power switches have soft switching capability, and the ZVS range under light load is expanded compared to existing OADM control, resulting in a significant promotion of DAB efficiency.

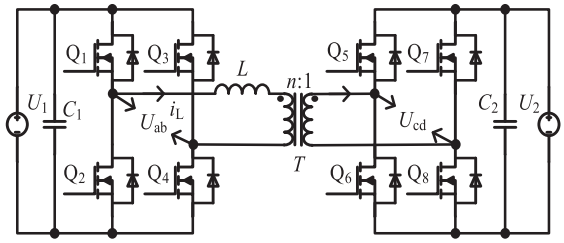

Fig. 1. Topology of DAB converter.

According to the comparative analysis with similar modulation schemes, the advantages of the proposed DVDM scheme can be summarized as follows.

1) Compared with other three degrees of freedom control, the proposed DVDM scheme actually control four variables, which improves the control performance without increasing the control complexity.
2) The proposed DVDM scheme not only broadens the ZVS range but also decreases the RMS current across the entire load range, effectively combining the advantages of the ADM and SDM schemes. The performance under light load can be significantly improved, while the high efficiency under heavy load is not affected.

The rest of this article is organized as follows. Section II introduces the working principle and mode classification of the proposed DVDM scheme. In Section III, the global optimal solution of DVDM scheme based on the peak-to-peak inductor current optimization is derived. Section IV compares the RMS current and soft switching characteristics of DVDM, FDM and OADM schemes. Section V conducts experimental verification. Finally, Section VI concludes this article.

II. Working Principle of Dual-Side Variable Duty Cycle Phase-Shift Modulation

As the topology of DAB converter shown in Fig. 1, two full-bridges on the primary and secondary sides are composed of four switches respectively, connected through a high-frequency transformer with the turns ratio of n and an inductor L. The midpoint output voltages of two full-bridges are U_{ab} and U_{cd}. L is the sum of transformer leakage inductance and series auxiliary inductance. U_1 represents the input voltage, and the output voltage is U_2. C_1 and C_2 are used as input and output filter capacitors respectively in the circuit. Specify f_s as the switching frequency and T_s as the switching period.

In order to better improve the efficiency and expand ZVS range of DAB especially in light load application, an ADM with three degrees of freedom is proposed. The main operation principle and mode classification of DVDM are introduced as follows.

The switches on both sides of the transformer are modulated with variable duty cycles, while the driving signals of the switches on the same bridge arm are complementary. The typical drive signal waveforms of DVDM scheme are shown in Fig. 2. The phase-shift ratio between the primary side switches Q_1 (Q_2) and Q_4 (Q_3) is defined as the inner phase-shift ratio D_1, and the

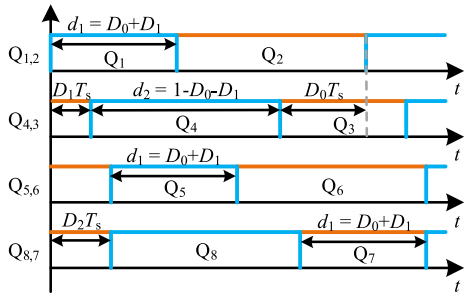

Fig. 2. Typical drive signal waveforms of the DVDM scheme.

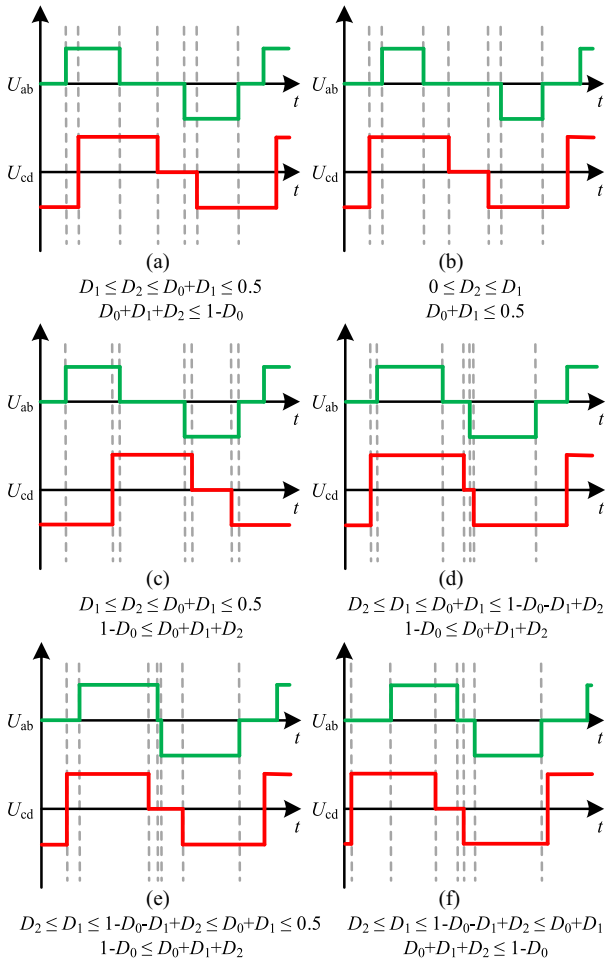

Fig. 3. Mode classification of DVDM scheme.

outer phase-shift ratio D_2 is the phase shift between Q_1 and Q_5. D_0 is defined as the phase-shift ratio between Q_1 and Q_3. In other words, the duty cycle of Q_1 can be expressed as D_0+D_1. The duty cycles of Q_3, Q_5, and Q_7 are all the same as Q_1.

Based on the unequal relationship between D_0, D_1, and D_2, there are six modes depicted in Fig. 3 and the boundary condition of them are listed respectively.

The conditions that $D_2 > D_0+D_1$, $D_2 > 1-D_0$ and $D_1 > 1-D_0-D_1+D_2$ are not considered, because the product of U_{ab} and U_{cd} will be less than 0 for a long time which leads to the increase of reactive power and transformer losses. Here, mode 1 to mode 3 in which the duty cycle of Q_1 is less than 50% ($D_0+D_1 \le 0.5$) are analyzed, while mode 4 to mode 6 are not considered as the power transmission capacity of them is weaker. The operating waveforms of mode 1 to mode 3 are described in Fig. 4.

TABLE I
EXPRESSIONS OF TRANSMISSION POWER UNDER DIFFERENT MODES

Mode	Transmission Power p^*
1	$4(-2D_0D_1-3D_1^2+4D_0D_2+6D_1D_2-3D_2^2)$
2	$8(-D_0D_1+2D_0D_2)$
3	$4(-1+4D_0-4D_0^2+2D_1-6D_0D_1-4D_1^2+2D_2+4D_1D_2-4D_2^2)$

Mode 1 is taken as an example to deduce the expression of inductor current and transmission power. In a switching period, the inductor current can be derived as

$$i_L(t) = \begin{cases} i_L(t_0) + \frac{nU_2}{L}(t-t_0) & t \in (t_0, t_1) \\ i_L(t_1) + \frac{U_1+nU_2}{L}(t-t_1) & t \in (t_1, t_2) \\ i_L(t_2) + \frac{U_1-nU_2}{L}(t-t_2) & t \in (t_2, t_3) \\ i_L(t_3) + \frac{-nU_2}{L}(t-t_3) & t \in (t_3, t_4) \\ i_L(t_4) & t \in (t_4, t_5) \\ i_L(t_5) + \frac{-U_1}{L}(t-t_5) & t \in (t_5, t_6) \\ i_L(t_6) + \frac{-U_1+nU_2}{L}(t-t_6) & t \in (t_6, t_7) \end{cases}. \quad (1)$$

According to the ampere-second balance principle, the integral of inductor current within one switching period is 0, that is

$$\int_0^{T_s} i_L(t)\, dt = 0. \quad (2)$$

The voltage transmission ratio is defined as $k = U_1/nU_2$. This article only considers the case of $k > 1$. The current base value i_N and transmission power base value P_N are defined as

$$\begin{cases} i_N = \frac{nU_2}{8f_sL} \\ P_N = \frac{nU_1U_2}{8f_sL} \end{cases}. \quad (3)$$

Therefore, the initial value of inductor current can be obtained as

$$i_L(t_0)^* = 8k\left(-D_0 + D_0^2 + D_0D_1\right) + 8\left(D_0 - D_0^2 + D_1 - D_1^2 - 2D_0D_1 - D_2\right). \quad (4)$$

The per unit value of transmission power can be calculated as

$$p^* = \frac{1}{P_NT_s}\int_{t_0}^{t_0+T_s} v_{AB} \times i_L(t)\, dt = 4\left(-2D_0D_1 - 3D_1^2 + 4D_0D_2 + 6D_1D_2 - 3D_2^2\right). \quad (5)$$

The other two modes can be calculated similarly. The obtained transmission power of different modes is given in Table I.

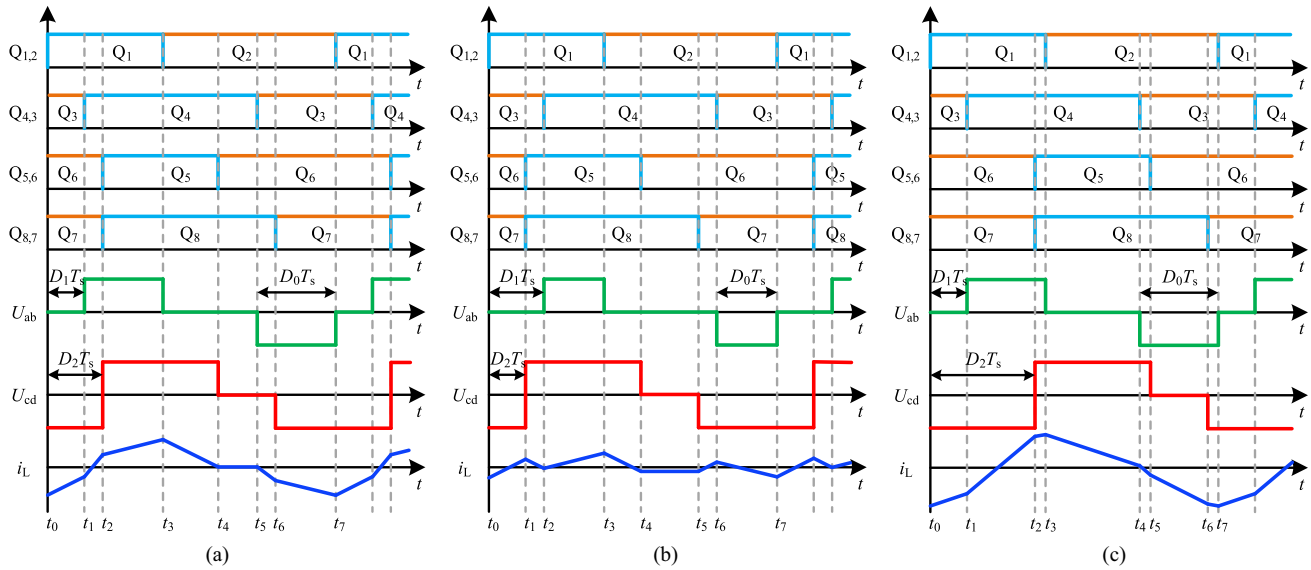

Fig. 4. Operating waveforms under three different modulation modes.

III. Optimization Control Strategy Based on Peak-to-Peak Inductor Current

When considering the losses of DAB, conduction loss and winding loss are directly proportional to the square of root mean square (RMS) current. Therefore, RMS current is frequently chosen as the optimization objective. However, the proposed DVDM has three degrees of freedom, which brings about complicated RMS current calculation and makes it difficult to be optimized. The peak-to-peak inductor current (i_{Lpp}) not only has a simple expression, but also reflects the variation law of RMS current. Hence, the control strategy in this section takes the peak-to-peak inductor current as the optimization objective.

According to the previous analysis, the minimum value of the inductor current in mode 1 occurs at t_0 as (4), and the maximum value occurs at t_3, which can be derived as

$$i_L(t_3)^* = 8\left[k\left({D_0}^2 + D_0D_1\right) + \left(-{D_0}^2 - {D_1}^2 - 2D_0D_1 + D_2\right)\right]. \tag{6}$$

Therefore, the expression of i^*_{Lpp} can be denoted as

$${i_{Lpp}}^* = 8\left[k\left(D_0\right) + \left(-D_0 - D_1 + 2D_2\right)\right]. \tag{7}$$

In order to reduce the switching losses and enhance the transmission efficiency, it is necessary to implement soft switching of switches, which means decreasing the voltage of the switch to 0 before it conducts. For mode 1, the soft switching conditions of all switches are $i_L(t_0) \le 0$, $i_L(t_1) \le 0$ (Q_4), $i_L(t_3) \ge 0$(Q_2), $i_L(t_5) \ge 0$ (Q_3), $i_L(t_2) \ge 0$ ($Q_{5,8}$), $i_L(t_4) \le 0$ (Q_6), $i_L(t_6) \le 0$ (Q_7). Thus, the soft switching constraints can be concluded as follows:

$$\begin{cases} k\left(-D_0\right) + \left(D_0 + 2D_1 - D_2\right) \le 0 \\ k\left(-D_0 + D_2 - D_1\right) + \left(D_0 + D_1\right) \ge 0 \\ \left(k-1\right)D_0 - D_1 = 0 \end{cases}. \tag{8}$$

When dealing with optimization problems with equality and inequality constraints, Lagrange multiplier method (LMM) and KKT conditions are extensively used methods [26]. KKT conditions describe some necessary conditions that the optimal solution should satisfy. Taking the transmission power model as the equality constraint, the soft switching conditions and mode boundary conditions above are inequality constraints, and i^*_{Lpp} is the optimization target. The optimization problem can be expressed as

$$\begin{aligned} \min \quad & {i_{Lpp}}^* = 8\left[k\left(D_0\right) + \left(-D_0 - D_1 + 2D_2\right)\right] \\ \text{s.t.} \quad & p^* = 4\left(-2D_0D_1 - 3{D_1}^2 + 4D_0D_2 + 6D_1D_2 - 3{D_2}^2\right) \\ & 0 \le D_1 \le D_2 \le D_0 + D_1 \le 0.5 \\ & D_0 + D_1 + D_2 \le 1 - D_0 \\ & k\left(-D_0\right) + \left(D_0 + 2D_1 - D_2\right) \le 0 \\ & k\left(-D_0 + D_2 - D_1\right) + \left(D_0 + D_1\right) \ge 0 \\ & \left(k-1\right)D_0 - D_1 = 0. \end{aligned} \tag{9}$$

Then, the corresponding Lagrange polar equation can be constructed

$$\begin{aligned} & E\left(D_0, D_1, D_2, \lambda\right) = 8\left[k\left(D_0\right) + \left(-D_0 - D_1 + 2D_2\right)\right] \\ & + \lambda\left[4\left(-2D_0D_1 - 3{D_1}^2 + 4D_0D_2 + 6D_1D_2 - 3{D_2}^2\right) - p^*\right]. \end{aligned} \tag{10}$$

Besides, the following KKT conditions need to be satisfied:

$$\begin{cases} \frac{\partial E}{\partial D_0} = 0, \frac{\partial E}{\partial D_1} = 0 \\ \frac{\partial E}{\partial D_2} = 0, \frac{\partial E}{\partial \lambda} = 0 \end{cases}. \tag{11}$$

TABLE II
EXPRESSIONS OF PEAK-TO-PEAK INDUCTOR CURRENT UNDER DIFFERENT MODES

Mode	Peak-to-peak Inductor Current $i_{\mathrm{Lpp}}{}^*$
1	$8\left[k\left(D_0\right)+\left(-D_0-D_1+2D_2\right)\right]$
2	$\max\begin{Bmatrix}8\left[k\left(D_0\right)+\left(-D_0\right)\right],8\left[k\left(D_0\right)+\left(-D_0-D_1+2D_2\right)\right],\\ 8\left[-k\left(D_0\right)+\left(D_0-D_1\right)\right],8\left[-k\left(D_0\right)+\left(D_0+D_1\right)\right]\end{Bmatrix}$
3	$8\left[k\left(D_0\right)+\left(-D_0-D_1+2D_2\right)\right]$

Therefore, the optimal solutions of three phase-shift ratios in mode 1 can be obtained as

$$\begin{cases} D_0 = \frac{\sqrt{p^*}}{2\sqrt{2\sqrt{k}-1}} \\ D_1 = \frac{\sqrt{k}-1\sqrt{p^*}}{2\sqrt{2}} \\ D_2 = \frac{\sqrt{k}-1\sqrt{p^*}}{2\sqrt{2}} \end{cases}. \tag{12}$$

Further, the expression of minimum i^*_{Lpp} with respect to the k and p^* under the optimal phase-shift ratio combination can be calculated as

$$i_{Lpp\min}{}^* = 4\sqrt{2}\sqrt{k-1}\sqrt{p^*}. \tag{13}$$

According to the boundary conditions of mode 1, the transmission power range of mode 1 is expressed as

$$0 \le p^* \le \frac{2k-2}{k^2}. \tag{14}$$

When DAB operates in mode 2, i^*_{Lpp} will get different expressions based on the unequal relationship of phase-shift ratios, making the analysis more complex. However, according to (12), the optimal phase-shift ratios of mode 1 satisfy $D_1 = D_2$, which is the boundary between mode 1 and mode 2. Therefore, the relationship of optimal solutions in mode 2 is also located at this boundary, and its optimal phase-shift ratio combination is identical with mode 1.

As for mode 3, the ZVS conditions are denoted as (15) shown at the bottom of this page.

The i^*_{Lpp} in mode 3 is the same as that in mode 1, and the expressions of i^*_{Lpp} under three modes are given in Table II. Since optimization control analysis of mode 3 is similar to mode 1, the optimized three phase-shift ratios of mode 3 are

$$\begin{cases} D_0 = \frac{1}{2} - \frac{(k-1)\sqrt{1-p^*}}{2\sqrt{k^2-2k+2}} \\ D_1 = \frac{(k-1)\sqrt{1-p^*}}{2\sqrt{k^2-2k+2}} \\ D_2 = \frac{1}{4} + \frac{(k-2)\sqrt{1-p^*}}{4\sqrt{k^2-2k+2}} \end{cases}. \tag{16}$$

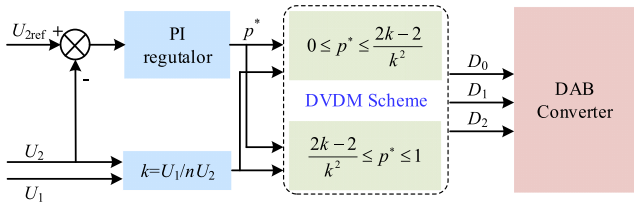

Fig. 5. Closed-loop control block diagram of DVDM scheme.

Hence, $i^*_{Lpp\min}$ is expressed as

$$i_{Lpp\min}{}^* = 4\left(k - \sqrt{(1-p^*)\left(k^2-2k+2\right)}\right). \tag{17}$$

The transmission power range of mode 3 is derived as follows:

$$\frac{2k-2}{k^2} \le p^* \le 1. \tag{18}$$

From (16), it can be found that D_1 and D_2 satisfy the relationship $D_1+D_2 = 0.5$, which indicates that the duty cycle of all switches remains constant at 0.5 and the optimization control under Mode 3 is an EPS control actually.

In summary, at high power range $p^*\in[(2k\text{-}2)/k^2,1]$, DAB operates in mode 3, while under the low power range $p^*\in[0, (2k\text{-}2)/k^2]$, DAB operates in mode 1 (mode 2). The optimal phase-shift ratio combination, corresponding transmission power range of DAB converter, $i^*_{Lpp\min}$ and duty cycle of all switches under mode 1 to mode 3 are given in Table III.

According to the analysis above, the closed-loop control of the system under DVDM scheme can be achieved by regulating the phase-shift ratio. Its closed-loop control block diagram is shown in Fig. 5.

Compared the detected output voltage U_2 with the reference voltage $U_{2\mathrm{ref}}$, the transmission power per unit value p^* can be obtained through the output of proportional integral controller and the sampling current. Under specific input and output voltages, the voltage transmission ratio and the mode boundary of the modulation scheme are definite. By comparing the real-time p^* with the mode boundary, the desired operating mode can be selected and D_0, D_1, and D_2 can be calculated. The optimal phase-shift ratios are used to generate PWM signals to control the switches of DAB converter, finally achieving the goal of the output voltage tracking. The closed-loop control process is implemented by the digital controller STM32G474RET6.

IV. CHARACTERISTIC COMPARISON ANALYSIS OF DIFFERENT MODULATION SCHEMES

To demonstrate the advantages of the DVDM scheme proposed in this article, in this section, comparison is conducted in terms of peak-to-peak inductor current, RMS current, and

$$\begin{cases} k\left(-D_0+{D_0}^2+D_0D_1\right)+\left(D_0-{D_0}^2+2D_1-{D_1}^2-2D_0D_1-D_2\right)\le 0 \\ k\left(-D_0+{D_0}^2+D_0D_1+D_2-D_1\right)+\left(D_0-{D_0}^2+D_1-{D_1}^2-2D_0D_1\right)\ge 0 \\ k\left({D_0}^2+D_0D_1\right)+\left(2D_0-{D_0}^2+D_1-{D_1}^2-2D_0D_1+D_2-1\right)\ge 0 \\ k\left(-2D_0+{D_0}^2+D_0D_1-D_1-D_2+1\right)+\left(-{D_0}^2-{D_1}^2-2D_0D_1\right)\le 0 \end{cases}. \tag{15}$$

TABLE III
TRANSMISSION POWER RANGE, OPTIMAL PHASE-SHIFT RATIO COMBINATION, $i_{\mathrm{Lpp\,MIN}}{}^{*}$ AND DUTY CYCLE OF ALL SWITCHES UNDER MODE 1 TO MODE 3

Mode	Transmission Power Range	Optimal Phase-shift Ratio Combination	$i_{\mathrm{Lppmin}}{}^{*}$	Duty cycle of Q_1, Q_3, Q_5, Q_7	Duty cycle of Q_2, Q_4, Q_6, Q_8
1(2)	$0 \le p^* \le \frac{2k-2}{k^2}$	$\begin{cases} D_0 = \frac{\sqrt{p^*}}{2\sqrt{2}\sqrt{k-1}} \\ D_1 = \frac{\sqrt{k-1}\sqrt{p^*}}{2\sqrt{2}} \\ D_2 = \frac{\sqrt{k-1}\sqrt{p^*}}{2\sqrt{2}} \end{cases}$	$4\sqrt{2}\sqrt{k-1}\sqrt{p^*}$	$\frac{k\sqrt{p^*}}{2\sqrt{2}\sqrt{k-1}}$	$1-\frac{k\sqrt{p^*}}{2\sqrt{2}\sqrt{k-1}}$
3	$\frac{2k-2}{k^2} \le p^* \le 1$	$\begin{cases} D_0 = \frac{1}{2} - \frac{(k-1)\sqrt{1-p^*}}{2\sqrt{k^2-2k+2}} \\ D_1 = \frac{(k-1)\sqrt{1-p^*}}{2\sqrt{k^2-2k+2}} \\ D_2 = \frac{1}{4} + \frac{(k-2)\sqrt{1-p^*}}{4\sqrt{k^2-2k+2}} \end{cases}$	$4\left(k-\sqrt{(1-p^*)(k^2-2k+2)}\right)$	$\frac{1}{2}$	$\frac{1}{2}$

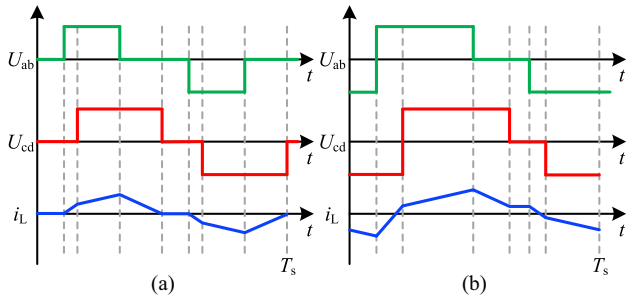

Fig. 6. Basic operating waveforms of DAB under FDM and OADM.

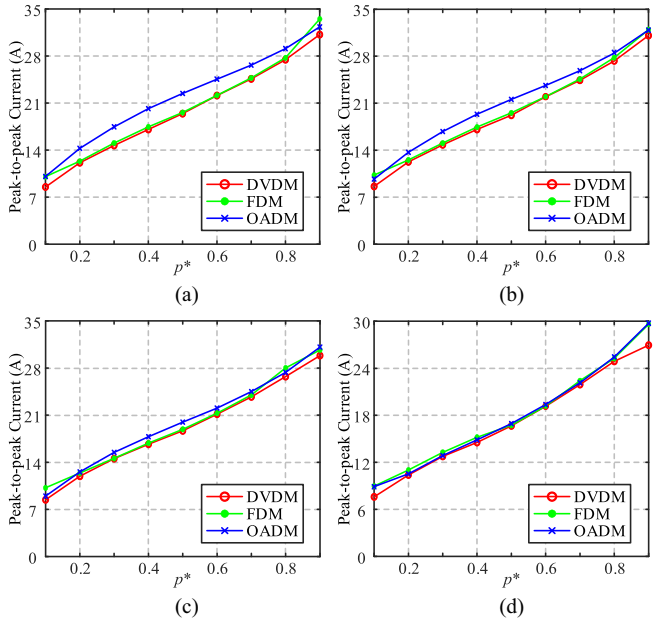

Fig. 7. Peak-to-peak inductor current comparison curves of DVDM, FDM and OADM when (a) $k = 2$, (b) $k = 1.75$, (c) $k = 1.5$, and (d) $k = 1.25$.

ZVS range among DVDM control, FDM control [15], and OADM control [24] under different voltage transmission ratio and transmission power.

FDM and OADM schemes both have three degrees of freedom. FDM control is a modulation strategy based on TPS optimization, and its operating waveforms are shown in Fig. 6(a). With the optimized inductor current stress, the secondary side inner phase-shift ratio is fixed to zero, and it only needs to adjust the primary side inner phase-shift ratio and outer phase-shift ratio, consequently its operation is relatively simple. OADM control is shown in Fig. 6(b). The duty cycles of its primary and secondary side full-bridges power switches vary independently. When the duty cycle is all 0.5, it is a form of SPS control.

A. Peak-to-Peak Inductor Current Comparison

OADM control and DVDM scheme are both optimized for the peak-to-peak inductor current. Therefore, the comparative analysis of i_{Lpp} under three modulation schemes is conducted first. Fig. 7 depicts the curves of i_{Lpp} changing with p^* under different values of k ($k = 2$, $k = 1.75$, $k = 1.5$, and $k = 1.25$).

It can be observed that when $k = 2$, i_{Lpp} under DVDM control is significantly reduced compared with OADM control. As the value of k approaches 1, the i_{Lpp} obtained by DVDM tends to be close to that of OADM, but it can still reach lower values in the full load range. The peak-to-peak inductor currents of FDM control and DVDM control are not apparently different at medium power range, while the optimization effect of DVDM control is extremely prominent at light and heavy load conditions, with i_{Lpp} under DVDM far lower than the other two modulation schemes. Therefore, in terms of optimizing the peak-to-peak inductor current, DVDM has the best effect, followed by FDM control, and the worst is OADM control.

B. RMS Current Comparison

High switch RMS current may increase the conduction loss of the power switch, thereby affecting the efficiency of DAB. Hence, fulfilling a lower inductor RMS current can help to reduce the switch RMS current and improve the performance

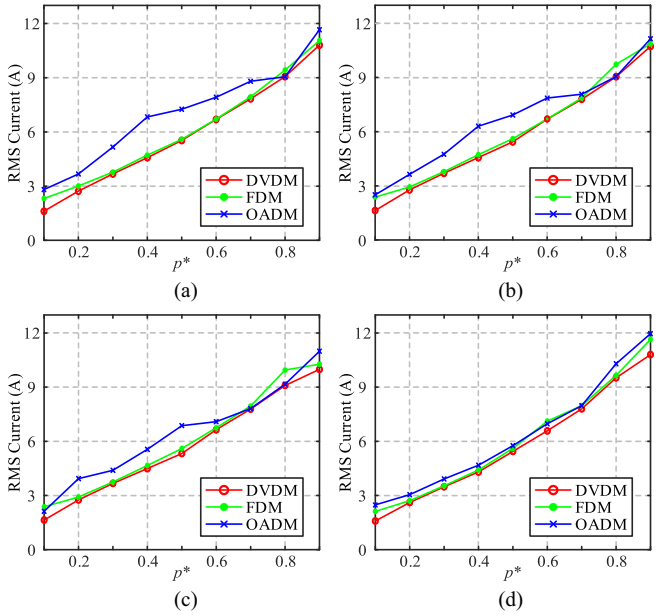

Fig. 8. Inductor RMS current comparison curves of DVDM, FDM and OADM when (a) $k = 2$, (b) $k = 1.75$, (c) $k = 1.5$, and (d) $k = 1.25$.

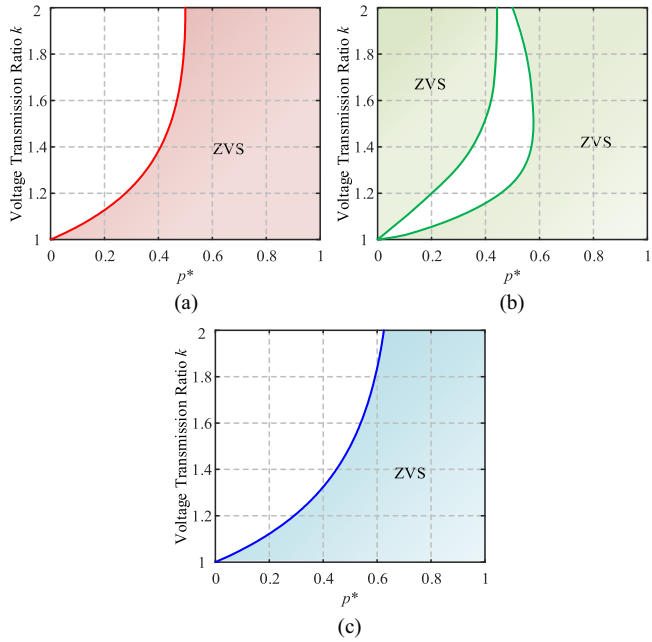

Fig. 9. ZVS range of DVDM, FDM and OADM over full power range.

of DAB. The comparison curves of inductor RMS current under different control strategies at $k = 2$, $k = 1.75$, $k = 1.5$, and $k = 1.25$ are given in Fig. 8. It can be seen from the diagram that in the low and medium power range, the RMS current of OADM scheme is evidently higher than that of DVDM and FDM schemes. Similar to the case of the peak-to-peak inductor current, the RMS current optimization effect of DVDM control is also significant compared to FDM control when the transmission power is extremely low or close to full load. In addition, the higher the degree of voltage mismatch, in other words, the larger the value of k, the more obvious the advantage of DVDM scheme on RMS current. In general, the optimization control strategy for the peak-to-peak inductor current in this article also effectively diminishes the RMS current value, which has better effect than OADM and FDM schemes.

C. ZVS Characteristic Comparison

With the increasing demand of high power density, the switching frequency is becoming higher and higher, hence the switching losses account for the main part of the circuit losses, and ZVS characteristic is one of the important factors to evaluate the converter performance.

In order to achieve zero voltage switching of switches, in addition to the inductor current direction at the switching moment, the inductor also requires to provide sufficient energy to make the junction capacitance of the switches fully discharged, which can be expressed as

$$\frac{1}{2}Li_L{}^2 > C_{\text{oss}}U^2 \tag{19}$$

where C_{oss} is the output capacitor of the switch.

For the switches of primary side, $U = U_1$, and for the switches of secondary side, $U = U_2$. According to (19), the ZVS ranges of three modulation schemes under different voltage transmission ratio and transmission power are plotted in Fig. 9. All switches in the colored area achieve soft switching, while in the blank area, at least two switches are either hard switching or partially ZVS conducting. Under FDM control, only Q_3 and Q_4 switches do not have soft switching capability in the low and medium power range. DVDM control and OADM control can make all switches realize ZVS in the medium and high power range, but their ZVS ranges are smaller than FDM control. Besides, the ZVS characteristics of DVDM are slightly better than OADM control.

In conclusion, the comparison of DVDM scheme with other modulation schemes is given in Table IV.

V. Experimental Results

In order to verify the above-mentioned theoretical analysis, a 100 kHz 50 V/25 V 10 A laboratory prototype is built as shown in Fig. 10. The electrical parameters and main components are listed, respectively, in Tables V and VI. The IPP083N10N5 is selected as the power switches of the primary and secondary sides, which has the advantages of fast switching speed, low on resistance, and low switching losses. To testify the advantages of DVDM scheme, the experimental results of DAB under DVDM, FDM, and OADM schemes at $k = 2$ are given, and the efficiency curves of the above three schemes are compared.

Fig. 11 gives the steady-state operating waveforms at different transmission power under DVDM control when $k = 2$ and Fig. 12 shows the voltage and drive signal of switches under DVDM control when $k = 2$, $p^* = 0.3$. It can be seen from the figure that when $p^* = 0.3$, DAB operates in the low power section with the same inner and outer phase-shift ratio, which means that Q_4 and Q_5 turn on simultaneously. The duty cycles of all switches are

TABLE IV
COMPARISON OF DVDM SCHEME WITH OTHER MODULATION SCHEMES

Modulation Scheme	Modulation Type	DOF	Optimization Objective	Constraint	ZVS Range	RMS Current
DVDM	EPS+ADM	3	Peak-to-Peak current	Mode Boundary+ZVS	Medium	Lowest
FDM in [15]	TPS	3	RMS current	Phase-Shift Ratio limitation	Wide	Relatively High
OADM in [24]	SPS+ADM	3	Peak-to-Peak current	Mode Boundary	Narrow	High

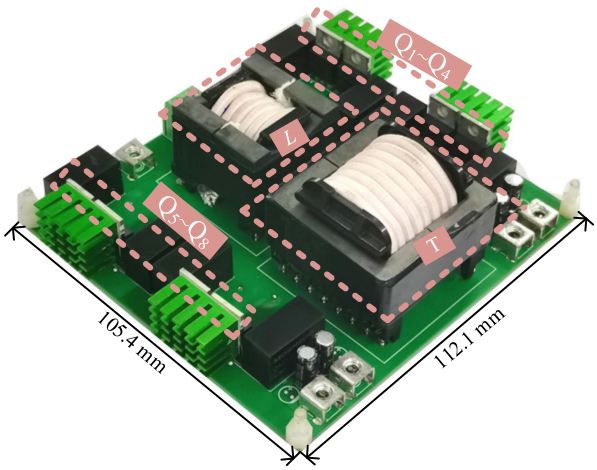

Fig. 10. DAB prototype.

TABLE V
DAB MAIN PARAMETERS

Parameters	Value
Input voltage U_1	50 V
Output voltage U_2	25 V
Switching frequency f	100 kHz
Input capacitor C_1	20 μF
Output capacitor C_2	20 μF
Voltage transmission ratio k	2
Rated power P	250 W

TABLE VI
MAIN COMPONENTS

Components	Model	Parameters
L	PQ3230/PC95	L = 6.25 μH
T	EE4215/PC95	n = 1, L_m = 18.5 μH
Q	IPP083N10N5	C_{oss} = 337 pF

not 50%, and except for Q_3 and Q_4, the other switches achieve soft switching. When $p^* = 0.6$ and $p^* = 0.8$, DAB operates in the high power range with a duty cycle of 50% for all switches and all switches implementing ZVS. Therefore, the working status and ZVS performance are consistent with theoretical analysis.

Figs. 13 and 14 show the working waveforms under different control strategies at $k = 2$, and $p^* = 0.2$ or $p^* = 0.7$, moreover, peak-to-peak inductor currents and RMS currents are also listed. The i_{Lpp} and $i_{L\mathrm{rms}}$ under DVDM are both the lowest, and the $i_{L\mathrm{rms}}$ is relatively close to that of FDM at $p^* = 0.7$. When $p^* = 0.2$, all switches under FDM control achieve ZVS, while under DVDM, only Q_3 and Q_4 do not realize zero voltage turn-ON, and only Q_1, Q_2, and Q_4 have soft switching performance under OADM control. When $p^* = 0.7$, all switches under the three controls achieve soft switching. Therefore, in line with the above analysis, DVDM has advantages in current optimization, and outperforms OADM control in the ZVS characteristics but not as good as FDM control.

The dynamic response waveform are shown in Fig. 15, which displays the voltage and current waveforms when the output power changes from 0.2 to 0.5 and then to 0.7. The results show that when the load changes, the proposed closed-loop control strategy can adjust the output power to the required value without obvious current and voltage overshoot. The proposed DVDM strategy does not have obvious negative impact on dynamic performance.

In order to better reflect the advantages of DVDM control, the efficiency of DAB under three modulation schemes over full load range at $k = 2$ and $k = 1.5$ is compared in Fig. 16. It can be spotted that, when $k = 2$, the transmission efficiency of DVDM, FDM, and OADM reaches the maximum value of 95.48%, 95.24%, and 94.07% at $p^* = 0.6$, respectively, while peak efficiency locates at $p^* = 0.5$ under $k = 1.5$. The efficiency of DVDM has prominent improvement overall compared to OADM and FDM, and under light load conditions, DVDM has most obvious promotion over FDM. Besides, the efficiency of DVDM is 2.12% higher than FDM at most and 1.76% higher than OADM at most. In conclusion, under different voltage ratios, DVDM control can achieve higher efficiency throughout the entire power range and the improvement is more obvious at light load.

Since the losses of DAB mainly come from the conduction loss and switching loss of power switches and the core loss and copper loss of transformer and series inductor, this article also analyzes the loss of different modulation schemes from these four parts. The conduction loss is related to the RMS current and ON-state resistance of the switch, and the copper loss is also proportional to the RMS current. The switching loss is associated with the energy when the switch is turned ON and turned OFF, while the core loss model can be constructed by the data manual of the core material and the modified Steinmetz formula. The power loss distribution diagram under $k = 2$ obtained from the above analysis is shown in Fig. 17. With the increase of transmission power, the core loss is basically invariable, but the proportion of conduction loss and copper loss increases gradually. Although there are two switches of DVDM scheme operate in critical soft switching state under light load, the current at turn-ON and turn-OFF time is low, resulting in lower switching loss compared to FDM. In contrast, the OADM scheme has a large number of hard-switching switches and the highest switching loss. Furthermore, due to the best RMS current optimization effect of DVDM scheme, the conduction loss and copper loss over the full load range is always at a relative low level.

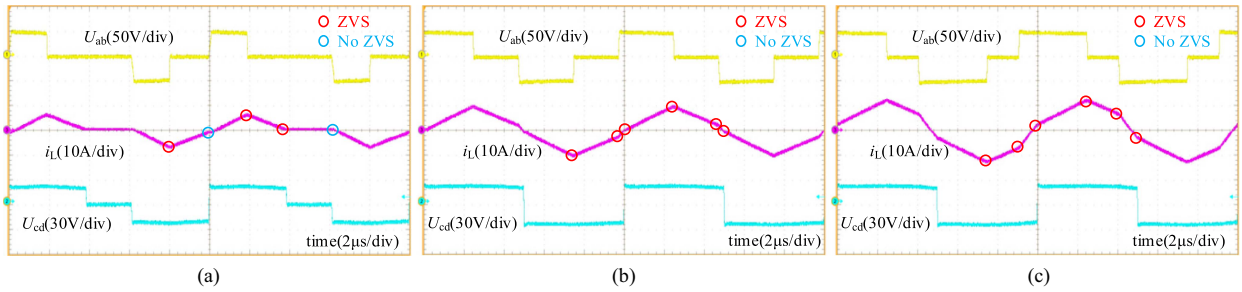

Fig. 11. Experimental waveforms of DVDM when $k = 2$. (a) $p^* = 0.3$. (b) $p^* = 0.6$. (c) $p^* = 0.8$.

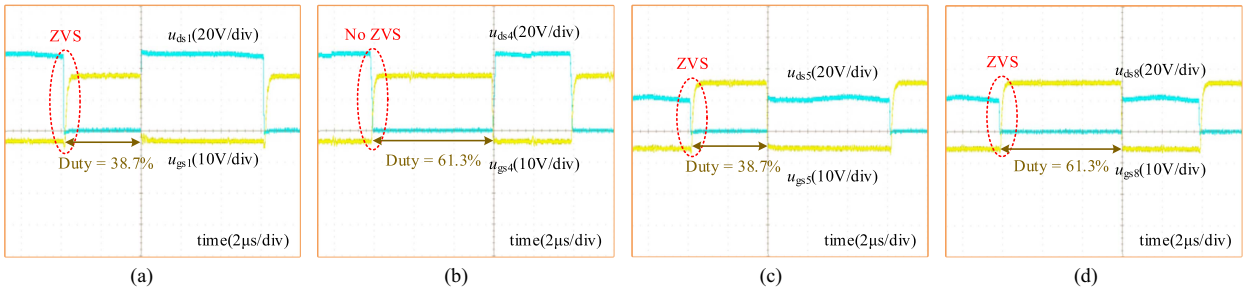

Fig. 12. Voltage and drive signal of switches under DVDM control when $k = 2$, $p^* = 0.3$. (a) Q_1. (b) Q_4. (c) Q_5. (d) Q_8.

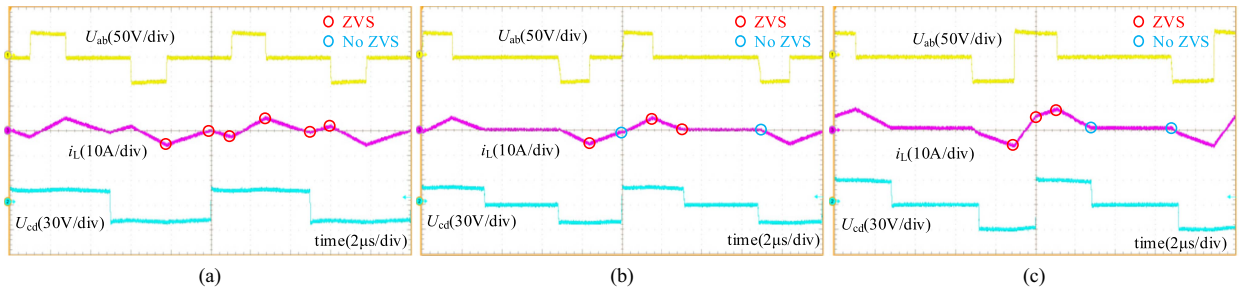

Fig. 13. Experimental waveforms of DVDM, FDM, and OADM when $k = 2$, $p^* = 0.2$. (a) FDM : $i_{\mathrm{Lpp}} = 12.4$A, $i_{\mathrm{Lrms}} = 2.638$A. (b) DVDM : $i_{\mathrm{Lpp}} = 12.0$A, $i_{\mathrm{Lrms}} = 2.39$A. (c) OADM : $i_{\mathrm{Lpp}} = 16.4$A, $i_{\mathrm{Lrms}} = 3.778$A.

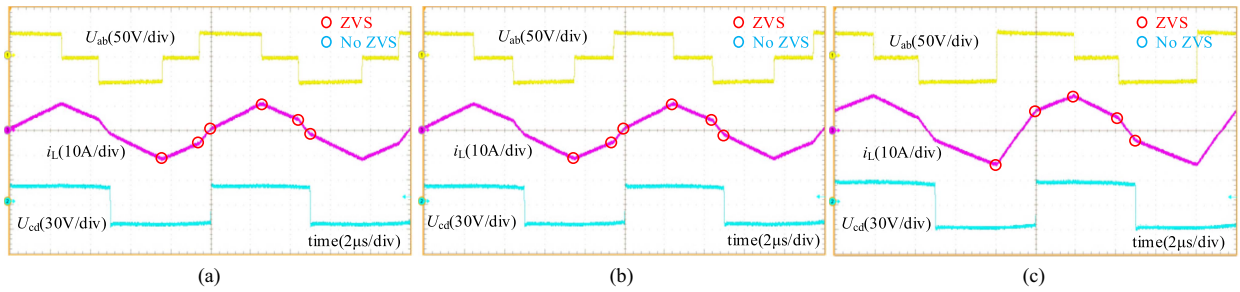

Fig. 14. Experimental waveforms of DVDM, FDM, and OADM when $k = 2$, $p^* = 0.7$. (a) FDM : $i_{\mathrm{Lpp}} = 24.0$A, $i_{\mathrm{Lrms}} = 7.08$A. (b) DVDM : $i_{\mathrm{Lpp}} = 23.6$A, $i_{\mathrm{Lrms}} = 6.996$A. (c) OADM : $i_{\mathrm{Lpp}} = 29.6$A, $i_{\mathrm{Lrms}} = 9.131$A.

VI. Conclusion

This article proposes a new DVDM scheme for DAB converter with three degrees of freedom based on EPS control and ADM control, in which the duty cycle of the switches on both sides of the transformer changes simultaneously. First, the basic working principle and operational characteristics of DVDM are analyzed. Then, taking the peak-to-peak inductor current of DAB as optimization objectives, the optimal control scheme of the full power range is obtained through LMM and KKT conditions. Finally, a 100 kHz, 250W DAB experimental prototype is built to verify the effectiveness of the scheme. Compared with OADM and FDM schemes, DVDM can achieve the lowest peak-to-peak inductor current and RMS current. The peak efficiency under

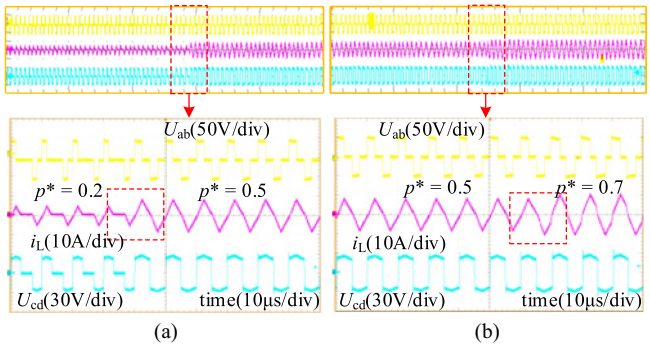

Fig. 15. Dynamic response waveforms. (a) $p^* = 0.2$ to $p^* = 0.5$. (b) $p^* = 0.5$ to $p^* = 0.7$.

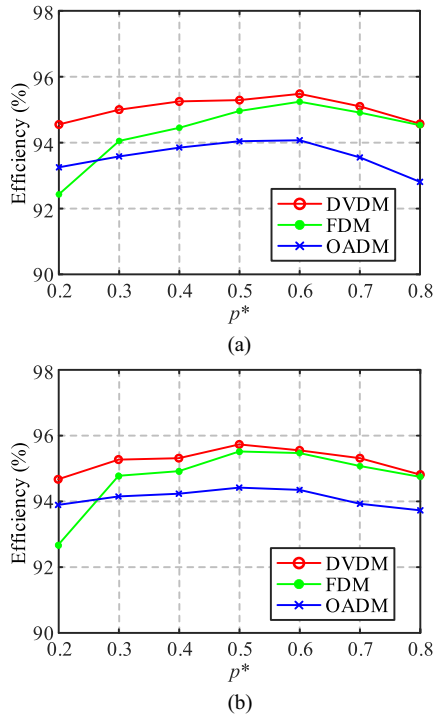

Fig. 16. Efficiency curves of DVDM, FDM and OADM when (a) $k = 2$ and (b) $k = 1.5$.

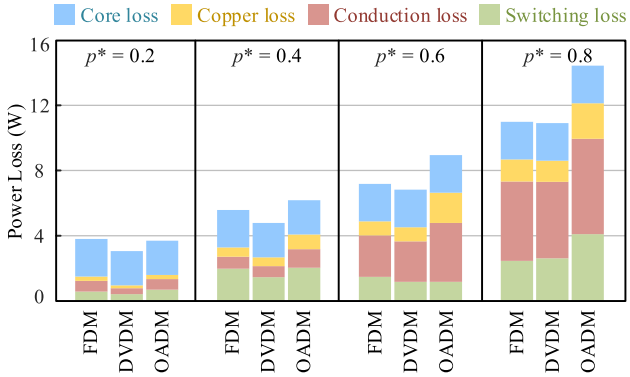

Fig. 17. Power loss distribution of DVDM, FDM and OADM when $k = 2$.

DVDM can reach 95.48%, which is up to 2.12% higher than the other two control strategies at most, and the improvement is most pronounced at light load. The experimental results are consistent with theoretical analysis.

REFERENCES

[1] T. Dragičević, X. Lu, J. C. Vasquez, and J. M. Guerrero, "DC microgrids—Part I: A review of control strategies and stabilization techniques," *IEEE Trans. Power Electron.*, vol. 31, no. 7, pp. 4876–4891, Jul. 2016.

[2] Y. Shi, R. Li, Y. Xue, and H. Li, "Optimized operation of current-fed dual active bridge DC–DC converter for PV applications," *IEEE Trans. Ind. Electron.*, vol. 62, no. 11, pp. 6986–6995, Nov. 2015.

[3] A. Kazemtarghi, S. Dey, A. Mallik, and N. G. Johnson, "Asymmetric half-frequency modulation in DAB to optimize the conduction and switching losses in EV charging applications," *IEEE Trans. Transp. Electrific.*, vol. 9, no. 3, pp. 4196–4210, Sep. 2023.

[4] L. Tarisciotti, A. Costabeber, L. Chen, A. Walker, and M. Galea, "Current-fed isolated DC/DC converter for future aerospace microgrids," *IEEE Trans. Ind. Appl.*, vol. 55, no. 3, pp. 2823–2832, May/Jun. 2019.

[5] X. Chen, G. Xu, H. Han, D. Liu, Y. Sun, and M. Su, "Light-load efficiency enhancement of high-frequency dual-active-bridge converter under SPS control," *IEEE Trans. Ind. Electron.*, vol. 68, no. 12, pp. 12941–12946, Dec. 2021.

[6] S. Bal, D. B. Yelaverthi, A. K. Rathore, and D. Srinivasan, "Improved modulation strategy using dual phase shift modulation for active commutated current-fed dual active bridge," *IEEE Trans. Power Electron.*, vol. 33, no. 9, pp. 7359–7375, Sep. 2018.

[7] X. Liu et al., "Novel dual-phase-shift control with bidirectional inner phase shifts for a dual-active-bridge converter having low surge current and stable power control," *IEEE Trans. Power Electron.*, vol. 32, no. 5, pp. 4095–4106, May 2017.

[8] Q. Bu, H. Wen, J. Wen, Y. Hu, and Y. Du, "Transient DC bias elimination of dual-active-bridge DC–DC converter with improved triple-phase-shift control," *IEEE Trans. Ind. Electron.*, vol. 67, no. 10, pp. 8587–8598, Oct. 2020.

[9] H. Shi, H. Wen, and Y. Hu, "Deadband effect and accurate ZVS boundaries of GaN-based dual-active-bridge converters with multiple-phase-shift control," *IEEE Trans. Power Electron.*, vol. 35, no. 9, pp. 9886–9903, Sep. 2020.

[10] B. Zhao, Q. Song, W. Liu, and W. Sun, "Current-stress-optimized switching strategy of isolated bidirectional DC–DC converter with dual-phase-shift control," *IEEE Trans. Ind. Electron.*, vol. 60, no. 10, pp. 4458–4467, Oct. 2013.

[11] H. Shi et al., "Minimum-backflow-power scheme of DAB-based solid-state transformer with extended-phase-shift control," *IEEE Trans. Ind. Appl.*, vol. 54, no. 4, pp. 3483–3496, Jul./Aug. 2018.

[12] J. Huang, Y. Wang, Z. Li, and W. Lei, "Unified triple-phase-shift control to minimize current stress and achieve full soft-switching of isolated bidirectional DC–DC converter," *IEEE Trans. Ind. Electron.*, vol. 63, no. 7, pp. 4169–4179, Jul. 2016.

[13] S. S. Muthuraj, V. K. Kanakesh, P. Das, and S. K. Panda, "Triple phase shift control of an LLL tank based bidirectional dual active bridge converter," *IEEE Trans. Power Electron.*, vol. 32, no. 10, pp. 8035–8053, Oct. 2017.

[14] N. Noroozi et al., "RMS current minimization in a SiC-based dual active bridge converter using triple-phase-shift modulation," *IEEE Trans. Ind. Electron.*, vol. 70, no. 7, pp. 7173–7182, Jul. 2023.

[15] W. Choi, K.-M. Rho, and B.-H. Cho, "Fundamental duty modulation of dual-active-bridge converter for wide-range operation," *IEEE Trans. Power Electron.*, vol. 31, no. 6, pp. 4048–4064, Jun. 2016.

[16] G. Chen, Z. Chen, Y. Chen, C. Feng, and X. Zhu, "Comprehensive analysis of asymmetric modulated dual-active-bridge converter and its hybrid control strategy," *IEEE J. Emerg. Sel. Topics Power Electron.*, vol. 10, no. 4, pp. 4218–4230, Aug. 2022.

[17] A. Tong, L. Hang, G. Li, X. Jiang, and S. Gao, "Modeling and analysis of a dual-active-bridge-isolated bidirectional DC/DC converter to minimize RMS current with whole operating range," *IEEE Trans. Power Electron.*, vol. 33, no. 6, pp. 5302–5316, Jun. 2018.

[18] O. M. Hebala, A. A. Aboushady, K. H. Ahmed, and I. Abdelsalam, "Generic closed-loop controller for power regulation in dual active bridge DC–DC converter with current stress minimization," *IEEE Trans. Ind. Electron.*, vol. 66, no. 6, pp. 4468–4478, Jun. 2019.

[19] H. Shi, H. Wen, J. Chen, Y. Hu, L. Jiang, and G. Chen, "Minimum-reactive-power scheme of dual-active-bridge DC–DC converter with three-level modulated phase-shift control," *IEEE Trans. Ind. Appl.*, vol. 53, no. 6, pp. 5573–5586, Nov./Dec. 2017.
[20] L. Deng, G. Zhou, Q. Bi, and N. Xu, "Online reactive power minimization and soft switching algorithm for triple-phase-shift modulated dual active bridge converter," *IEEE Trans. Ind. Electron.*, vol. 70, no. 3, pp. 2543–2555, Mar. 2023.
[21] S. Hu, X. Li, and A. K. S. Bhat, "Operation of a bidirectional series-resonant converter with minimized tank current and wide ZVS range," *IEEE Trans. Power Electron.*, vol. 34, no. 1, pp. 904–915, Jan. 2019.
[22] S. Chakraborty and S. Chattopadhyay, "Minimum-RMS-current operation of asymmetric dual active half-bridge converters with and without ZVS," *IEEE Trans. Power Electron.*, vol. 32, no. 7, pp. 5132–5145, Jul. 2017.
[23] S. Chakraborty and S. Chattopadhyay, "Fully ZVS, minimum RMS current operation of the dual-active half-bridge converter using closed-loop three-degree-of-freedom control," *IEEE Trans. Power Electron.*, vol. 33, no. 12, pp. 10188–10199, Dec. 2018.
[24] D. Mou et al., "Optimal asymmetric duty modulation to minimize inductor peak-to-peak current for dual active bridge DC–DC converter," *IEEE Trans. Power Electron.*, vol. 36, no. 4, pp. 4572–4584, Apr. 2021.
[25] G. Chen, Z. Chen, Y. Chen, C. Feng, and X. Zhu, "Asymmetric phase-shift modulation strategy of DAB converters for improved light-load efficiency," *IEEE Trans. Power Electron.*, vol. 37, no. 8, pp. 9104–9113, Aug. 2022.
[26] C. Song, A. Sangwongwanich, Y. Yang, Y. Pan, and F. Blaabjerg, "Analysis and optimal modulation for 2/3-level DAB converters to minimize current stress with five-level control," *IEEE Trans. Power Electron.*, vol. 38, no. 4, pp. 4596–4612, Apr. 2023.

Shanshan Gao (Senior Member, IEEE) was born in Heilongjiang, China, in 1992. She received the B.S., M.S., and Ph.D. degrees in electrical engineering from the Harbin Institute of Technology (HIT), Harbin, China, in 2015, 2017, and 2021, respectively.

From 2022 to 2024, she was an Assistant Professor with the Department of Electrical and Electronics Engineering, Harbin Institute of Technology. Since 2024, she has been an Associate Professor with the School of Electrical Engineering and Automation, HIT. From 2020 to 2021, she was a visiting Ph.D. with Technical University of Denmark. Her research interests include high frequency dc–dc converters and LED lighting systems.

Jiaran Xu was born in Jiangxi Province, China, in 2002. She received the B.S. degree in electrical engineering in 2024 from Harbin Institute of Technology, China. She is currently working toward the M.S. degree in electrical engineering from Harbin Institute of Technology.

Her research interests include high frequency dc–dc converters.

Yijie Wang (Senior Member, IEEE) was born in Heilongjiang Province, China, in 1982. He received the B.S., M.S., and Ph.D. degrees in electrical engineering from Harbin Institute of Technology, Harbin, China, in 2005, 2007 and 2012, respectively.

From 2012 to 2014, he was a Lecturer with the Department of Electrical and Electronics Engineering, Harbin Institute of Technology. From 2014 to 2017, he was an Associate Professor with the Department of Electrical and Electronics Engineering, Harbin Institute of Technology. Since 2017, he has been a Professor with the Department of Electrical and Electronics Engineering, Harbin Institute of Technology. His interests include dc–dc converters, soft-switching power converters, power factor correction circuits, digital control electronic ballasts, and LED lighting systems.

Dr. Wang is an Associate Editor for IEEE TRANSACTIONS ON INDUSTRIAL ELECTRONICS, IEEE ACCESS, *IET Power Electronics,* and *Journal of Power Electronics*.

Xiangjun Zhang (Member, IEEE) was born in Shandong Province, China, in 1971. He received the B.S. degree in welding from Xi'an Jiao tong University, Xi'an, China, in 1993, the M.S. degree in welding from the Harbin Welding Institute, Harbin, China, in1999, and the Ph.D. degree in electrical engineering from the Harbin Institute of Technology, Harbin, China, in 2006.

From 2006 to 2013, he was a Lecturer with the Department of Electrical and Electronics Engineering, Harbin Institute of Technology, where he has been an Associate Professor since 2013. His research interests include the areas of electronic ballast, power factor correction circuits, high-power converters, and light emitting diode lighting systems.

Jianxing Liu (Senior Member, IEEE) received the B.S. degree in mechanical engineering and the M.E. degree in control science and engineering from the Harbin Institute of Technology, Harbin, China, in 2004 and 2010, respectively, and the Ph.D. degree in automation from the Technical University of Belfort-Montbellard, Belfort, France, in 2014.

He is currently a Professor with the Department of Control Science and Engineering, Harbin Institute of Technology. His current research interests include sliding mode control, nonlinear control and observation, industrial electronics, and renewable energy solutions.

Dr. Liu is currently an Associate Editor for several journals, including IEEE/CAA Journal of Automatica Sinica, IEEE TRANSACTIONS ON CIRCUITS AND SYSTEMS II: EXPRESS BRIEFS, IEEE SYSTEMS JOURNAL, NONLINEAR DYNAMICS, *ISA Transactions*, and IEEE JOURNAL OF EMERGING AND SELECTED TOPICS IN INDUSTRIAL ELECTRONICS. He is currently an Associate Editor of the Conference Editorial Board, IEEE Control Systems Society.

Cong Huang was born in Hubei, China, in 1992. He received the M.S., and Ph.D. degrees in mechanical engineering from the Harbin Institute of Technology (HIT), Harbin, China, in 2017, and 2022, respectively.

He is currently a Post-doctoral Researcher with the School of Mechatronics Engineering, HIT. His research focuses on wearable and flexible electronics.

Dianguo Xu (Fellow, IEEE) was born in Heilongjiang, China, in 1960. He received the B.S. degree in control engineering from Harbin Engineering University, Harbin, China, in 1982, and the M.S. and Ph.D. degrees in electrical engineering from Harbin Institute of Technology (HIT), Harbin, China, in 1984 and 1989, respectively.

In 1984, he was with the Department of Electrical Engineering, HIT, as an Assistant Professor. Since 1994, he has been a Professor with the Department of Electrical Engineering, HIT. He was the Dean of School of Electrical Engineering and Automation, HIT, from 2000 to 2010. He is currently the Vice President of HIT. He has authored or coauthored more than 600 technical papers. His research interests include renewable energy generation technology, power quality mitigation, sensorless vector controlled motor drives, and high performance servo system.

Dr. Xu is currently an Associate Editor for IEEE TRANSACTIONS ON INDUSTRIAL ELECTRONICS, IEEE TRANSACTIONS ON POWER ELECTRONICS, and IEEE JOURNAL OF EMERGING AND SELECTED TOPICS IN POWER ELECTRONICS. He is currently the Chairman of IEEE Harbin Section.